# Improving solar water-splitting performance of LaTaON$_2$ by bulk defect control and interface engineering

Huiting Huang[a], Jianyong Feng[a], Hongwei Fu[a], Bowei Zhang[b], Tao Fang[a], Qinfeng Qian[a], Yizhong Huang[b,*], Shicheng Yan[a], Junwang Tang[c], Zhaosheng Li[a,*], Zhigang Zou[a]

[a] Collaborative Innovation Center of Advanced Microstructures, National Laboratory of Solid State Microstructures, and College of Engineering and Applied Sciences, Nanjing University, Nanjing 210093, PR China
[b] School of Materials Science and Engineering, Nanyang Technological University, 639798, Singapore
[c] Department of Chemical Engineering, University College London, Torrington Place, London, WC1E 7JE, United Kingdom

## ARTICLE INFO

## ABSTRACT

Particle-assembled photoanode films for solar water splitting are often subjected to serious electron-hole recombination, thus exhibiting low solar-to-hydrogen efficiency. The construction of efficient particle-assembled photoanode remains a challenge. Here, taking LaTaON$_2$ particle-assembled photoanode as a model, bulk defect control and interface engineering were introduced to reduce the electron-hole recombination. As a result, the solar photocurrent of LaTaON$_2$ achieves 2.1 mA cm$^{-2}$ at 1.6 V$_{RHE}$ after the modification of CoO$_x$, an order of magnitude greater than the previously-reported value of 0.15 mA cm$^{-2}$. This dramatic enhancement is mainly ascribed to increased bulk electrical conductivity, and less back reactions on the conductive substrates, as well as facilitated hole transfer to reaction sites. This study may provide guidelines for the construction of highly efficient particle-assembled photoanode films.

## 1. Introduction

Since Fujishima and Honda uncovered a way to decompose water into oxygen and hydrogen via a TiO$_2$ photoanode absorbing UV irradiation [1], photoelectrochemical (PEC) water splitting has never lost its unique attraction to researchers all over the world [2–5]. Addressing the issue of dwindling fossil fuels that restricts our sustainable development, photoelectrochemical (PEC) cells for water splitting offers us an alternative to convert solar energy into fuels [6–9]. On one hand, PEC cells require suitable photoelectrodes, which should absorb a large proportion of the solar spectrum accompanying by an energy band that straddles both water reduction and oxidation potentials [10–14]. Intense efforts have been made to achieve the full potential of WO$_3$ (2.8 eV) [15–18], BiVO$_4$ (2.4 eV) [19–22] and α-Fe$_2$O$_3$ (2.1 eV) [23–29] due to their narrower bandgap than TiO$_2$ (3.0 ~ 3.2 eV), in order to extend the absorption edge for high solar-to-hydrogen efficiency. Recently, a class of (oxy)nitrides, including Ta$_3$N$_5$, LaTiO$_2$N, BaTaO$_2$N and LaTaON$_2$, has brought new possibility for efficient photoanodes due to their suitable bandgaps (1.8 ~ 2.1 eV) and energetics for unassisted water splitting [30–33].

On the other hand, a tandem PEC cell is needed to make full use of solar irradiation. In such a cell, transparent conductive substrates are indispensable for supporting the top photoanode, which permits the unabsorbed light to pass through and to be absorbed by the bottom photocathode. As for the (oxy)nitrides, the harsh synthetic conditions (NH$_3$ flow and relatively high synthetic temperature) make it difficult to realize in-situ growth on transparent conductive substrates. Electrophoretic deposition seems to be one of the best methods for fabricating these particle-assembled films of (oxy)nitride photoanodes with transparent conductive substrates [34,35].

However, the PEC performances of these particle-assembled photoanodes are always limited by electron-hole recombination at the particle (or grain) boundaries in the bulk, and the substrate/photoanode interface, as well as the photoanode/catalyst interface. In recent work, particle-assembled LaTaON$_2$ photoanodes have produced ca. 0.15 mA cm$^{-2}$ of solar water-splitting photocurrent at 1.6 V$_{RHE}$ [33], even though LaTaON$_2$ has a feasible bandgap (absorption up to ca. 630 nm) and a maximum theoretical photocurrent of ca. 15 mA cm$^{-2}$ under AM 1.5G (100 mW cm$^{-2}$) simulated solar irradiation. It is still a challenge to build up efficient particle-assembled photoanodes.

In this study, taking LaTaON$_2$ as an example, we have discussed how to construct efficient particle-assembled photoanodes by bulk defect control and interface engineering, which have been introduced to increase the bulk electrical conductivity. As a result, the solar

photocurrent (at 1.6 $V_{RHE}$) of LaTaON$_2$ has increased by 14 times in comparison with our previous report [33].

## 2. Experimental section

### 2.1. Synthesis of LaTaON$_2$ particles

A method described as flux-assisted ammonolysis was adopted to synthesize LaTaON$_2$ particles. With KCl as the flux additive, the LaTaO$_4$ precursor prepared by the polymerized complex (PC) method was heated at 950 °C for 10 h under a flow of NH$_3$ (600 mL min$^{-1}$). The above procedure was repeated three times with an intermediate wash and desiccation. In a typical procedure, about 1 g LaTaO$_4$ precursor was thoroughly ground in an agate mortar with an equal weight of KCl. After each procedure of flux-assisted ammonolysis, the obtained powder was washed several times with distilled water and then dried at 80 °C overnight. For the precursor prepared by the polymerized complex (PC) method, a stoichiometric amount of TaCl$_5$ (0.01 mol) and La(NO$_3$)$_3$·6H$_2$O (0.01 mol) were dissolved in methanol. Then citric acid (0.15 mol) and ethylene glycol (0.6 mol) were added to the solution. The transparent solution thus obtained was kept at 120 °C with stirring to promote polymerization. It was then transferred to an oven at 200 °C overnight until a dark brown resin was obtained. To remove the excess carbon, the dark brown resin was kept at 600 °C for 10 h. Then the amorphous white powder was sintered at various temperatures (1150 °C, 1250 °C, 1350 °C and 1450 °C) for another 10 h. Thus, the LaTaON$_2$ particles derived from precursors prepared by the polymerized complex method are denoted as PC1150, PC1250, PC1350 and PC1450, respectively.

### 2.2. Fabrication of particle-assembled LaTaON$_2$ photoanodes

LaTaON$_2$ particle-assembled photoanodes were fabricated via electrophoretic deposition (EPD), followed by a post-necking treatment. In a typical procedure, a suspension of acetone (25 mL) with 20 mg LaTaON$_2$ particles and 5 mg iodine was available for electrophoretic deposition after being sonicated for 10 min. Two parallel conductive substrates (F doped tin oxide, FTO) with a distance of approximate 1 cm were immersed in the suspension described above. After being kept at a bias of 10 V for 2 min, the LaTaON$_2$ coating, about 1 cm$^2$, was obtained. The coated substrates were dried at room temperature, followed by several episodes of a necking procedure with 30 μL TiCl$_4$ in methanol (10 mM) drip and a short-term heat treatment at 200 °C in between. The LaTaON$_2$ photoanodes were finally obtained after a heat treatment in an NH$_3$ flow at 440 °C for 30 min.

### 2.3. Photoelectrodeposition of CoO$_x$ on LaTaON$_2$ photoanodes with or without post heat treatment

A 500 W xenon lamp (USHIO Optical ModuleX) equipped with a cut-off filter (λ ≥ 420 nm) was used as the light source. The intensity was adjusted to 30 mW cm$^{-2}$ measured by a Newport 91150 calibrated reference cell. To make up the electroplating bath, 0.2249 g CoSO$_4$·7H$_2$O and 0.3140 g CH$_3$COOK were dissolved in 80 mL distilled water. The photoelectrodeposition was carried out in a three-electrode system with the fabricated LaTaON$_2$ photoanode as the working electrode while a Pt foil and a saturated calomel electrode (SCE) acted as the counter electrode and the reference electrode, respectively. The chronopotential method was used to conduct the photoelectrodeposition at an anodic current of 40 μA with duration of 100 s, during which the illumination was on for 80 s and off for the remaining 20 s. After the photoelectrodeposition, the photoanode was washed with distilled water and dried in air. For the heat treatment, the CoO$_x$-modified photoanodes were calcined at 300 °C for 30 min in different atmospheres (air, N$_2$, NH$_3$). Thus, the treated CoO$_x$ modified photoanodes are denoted as CoO$_x$(Air)/LaTaON$_2$, CoO$_x$(N$_2$)/LaTaON$_2$ and

CoO$_x$(NH$_3$)/LaTaON$_2$ corresponding to the sintering atmosphere, while the as-synthesized CoO$_x$ modified photoanodes are denote as CoO$_x$/LaTaON$_2$.

### 2.4. Photoelectrochemical characterization of the photoanodes

All the electrochemical measurements were carried out in a three-electrode system, which was the same configuration as the settings for the photoelectrodeposition, except that 1 M NaOH aqueous solution (pH = 13.6) served as the electrolyte. Unless otherwise specified, the potentials are reported against the reversible hydrogen electrode (RHE), which is expressed in Equation (1):

$$E_{RHE} = E_{SCE} + 0.242 \ V + 0.059 \times pH \tag{1}$$

where pH is the pH value of the specific electrolyte. As for the light sources, a 500 W xenon lamp equipped with a cut-off filter (λ ≥ 420 nm), providing visible light irradiation, and the Oriel Sol3A Class AAA Solar Simulator, offering AM 1.5 G simulated sunlight irradiation with a Newport 91150 reference cell calibrating to 100 mW cm$^{-2}$, were used for the PEC measurements. A black mask, in the middle of which was a circular window with a diameter of 6 mm, was used to confirm the same irradiated area of each measurement and the corresponding photocurrent densities were then normalized to 1 cm$^2$. To obtain the incident photon-to-current efficiency (IPCE), the xenon lamp equipped with band pass filters was used as the monochromatic light irradiation, the light intensity of which was measured by a photometer (Newport, 840-C, USA). The incident photon-to-current efficiency was calculated according to Equation (2):

$$IPCE (\%) = \frac{1240 \ (V \ nm) \times Photocurrent \ density \ (mA \ cm^{-2})}{Incident \ light \ intensity \ (mW \ cm^{-2}) \times Wavelength \ (nm)} \times 100 \tag{2}$$

The product of solar water splitting was analyzed using an Agilent 490 Micro GC.

### 2.5. Characterization of the LaTaON$_2$ particles and photoanodes

The XRD patterns of all the LaTaON$_2$ particles were collected on a powder X-ray diffractometer (XRD, Rigaku UltimaIII) with Cu K$_\alpha$ radiation (λ = 1.54056 Å) in the step-wise mode. To obtain the optical absorption spectra of the LaTaON$_2$ particles, a UV–vis (UV-VIS) spectrophotometer (Shimadzu, UV–vis 2550) was used to conduct the measurements. The morphology of the LaTaON$_2$ particles and particle-assembled photoanodes was collected via a field-emission scanning electron microscopy (FE-SEM, Nova NanoSEM 230, FEI). For these SEM measurements, no conductive coating was deposited on the particles/photoanodes. The Co mappings were collected on another scanning electron microscopy (Zeiss Ultra 55). The electrical conductivity was obtained by a four-wire method in a home-made measurement device. The XPS experiments were conducted on a K-Alpha X-ray Photoelectron Spectrometer System (Thermo Fisher Scientific). To observe the distribution and configuration of CoO$_x$ on the photoanode, particles were dispersed in ethanol via ultrasonication, which were then examined using TEM (JEOL 2100F) at the electron beam energy of 200 KeV.

## 3. Results and discussion

All LaTaON$_2$ powders were synthesized via flux-assisted ammonolysis with KCl as the flux [36,37]. Compared with our previous report [33], the precursors for the same route were obtained via the polymerized complex (PC) method instead of the La$_2$O$_3$ + Ta$_2$O$_5$ mixture and were calcined at various temperatures. Details of the synthesis procedure were described in the experimental section. All the samples are identical to the perovskite-type LaTaON$_2$ corresponding to JCPDS file PDF#47-1366, confirmed by X-ray diffraction (XRD) patterns, as

shown in Fig. S1 in Supporting Information. Moreover, the as-synthesized $LaTaON_2$ powders exhibit an analogous absorption edge up to ca. 630 nm with an indirect bandgap of ca. 1.9 eV, as shown in Fig. S2 in Supporting Information, consistent with previous reports [33,38–40]. The electrophoretic deposition method was adopted to fabricate particle-assembled photoanode films. After a post-necking procedure including the dripping of $TiCl_4$ and a following heat treatment under $NH_3$, the $LaTaON_2$ photoanodes were ready for characterization. The as-fabricated $LaTaON_2$ photoanodes were denoted as PC1150, PC1250, PC1350 and PC1450 according to their various precursors.

Scanning electron microscopy (SEM) was used to obtain morphological characteristics of the sample powders and the as-fabricated photoanodes. With KCl as additive, all particles have a round smooth surface, as shown in Fig. S3 in Supporting Information. The $LaTaON_2$ particles are dispersed individual particles when the corresponding precursor is sintered at no more than 1250 °C. In the cases of PC1350 and PC1450, porous microparticles of several micrometers are formed. During the process of ammonolysis, part of the $O^{2-}$ ions in the oxide precursors is substituted by the $N^{3-}$ ions. To achieve the final stage of charge balance, three $O^{2-}$ are replaced by two $N^{3-}$ [38]. While being ammonolyzed at a high temperature, the oxide precursors are infiltrated within the molten salt, where the oxide is heated more evenly and the tension originating from the substitution seems to release. A topotaxial conversion happens during the high-temperature ammonolysis for the precursors sintered at higher temperatures, as in the case of 1350 °C and 1450 °C. The photoanodes by electrophoretic deposition (EPD) are particle-assemble films of the corresponding sample powder, as shown in Fig. 1. For all the photoanodes, some nearly transparent films attached to the $LaTaON_2$ particles are $TiO_x$ formed after the post-necking procedure [41]. The bottom of the PC1350 photoanode is filled with nanoparticles, while the PC1450 photoanode is with rare nanoparticles covering the substrate shown in Fig. S4.

Fig. 2a illustrates the photocurrent-potential characteristics of the particle-assembled photoanodes. The PC1150 photoanode shows water-splitting photocurrent of $0.25\,mA\,cm^{-2}$ at $1.6\,V_{RHE}$. As the sintering temperature of the precursor is increased to 1250 °C, the photocurrent of the PC1250 photoanode is only $0.12\,mA\,cm^{-2}$ at $1.6\,V_{RHE}$. In contrast, a photocurrent of $0.58\,mA\,cm^{-2}$ at $1.6\,V_{RHE}$ is achieved by the PC1350 photoanode. It should be noted that the samples PC1350 and PC1450 settled easily, while the suspensions of the first two were quite stable during the process of electrophoretic deposition.

The mean grain sizes of various $LaTaON_2$ samples are gained by performing the Scherrer equation on the (2 0 0) peak according to their

XRD patterns, as shown in Fig. S1 in Supporting Information. As shown in Fig. 2b, all the samples possess similar mean grain size, about 30–40 nm. Based on the morphological characteristics of the particle-assembled photoanodes, the mean grain sizes of the samples and their corresponding photocurrents at $1.6\,V_{RHE}$, as shown in Fig. 1Figs. 1 and Fig. 22b, the variation of the photocurrents may not be ascribed to charge transport in the $LaTaON_2$ crystalline grain. One critical factor that retards the conductive path for charged carriers is the grain (or particle) boundaries, as reported in the previous work [41]. More specifically, the hindrance of charged carriers mainly originates from the particle boundaries and the grain boundaries of the particles, which would be reflected by bulk electrical conductivity. The bulk electrical conductivity of $LaTaON_2$ powders were measured by a standard four-probe method [42]. Compared to ca. $2\,\mu S\,m^{-1}$ of PC1150 and PC1250, the electrical conductivity of PC1350 increases by about 75% to $3.5\,\mu S\,m^{-1}$ under the given pressures. The electrical conductivity of PC1450 increases from ca. $2.4\,\mu S\,m^{-1}$ under 1 MPa to ca. $3\,\mu S\,m^{-1}$ under 3 MPa. Compared with the PC1350 photoanode, as shown in Fig. S4 in Supporting Information, the bare conductive substrate of PC1450 photoanode would lead to a severe back reaction, which would impair the photocurrent [43]. Therefore, the highest bulk electrical conductivity of PC1350 and well covered substrate with suppressed back reaction results in the highest photocurrent among these samples.

Mott-Schottky tests have been conducted in the dark to obtain their flat band positions and the relative difference of the carrier densities. As shown in Fig. 2d, all the $LaTaON_2$ photoanodes possess similar flat band positions, slightly above $0\,V_{RHE}$ (more details can be found in Fig. S5 in Supporting Information), which explains the low activity of $H_2$ evolution in the case of a powdered photocatalyst system [33,40]. The similarity in flat band position may explain the similar photo-response of the different $LaTaON_2$ photoanodes shown in Fig. 2a. According to the Mott-Schottky equation, a lower slope of the curve corresponds to a higher carrier density of an n-type semiconductor [44,45]. Thus, the PC1350 possesses the highest carrier density among these samples, while the PC1150 has slightly lower carrier density but higher than PC1250 and PC1450. The variation of the carrier density is consistent with the photocurrent of the different $LaTaON_2$ photoanodes. PC1350 possesses the highest photocurrent at high bias with the highest carrier density, while PC1150 has lower photocurrent with a lower carrier density. The PC1250 and PC1450 have the similar lowest carrier density, which results in a similar photocurrent at high bias. In addition, with the bulk electrical conductivities of the samples, the carrier density further supports the different PEC performances of the $LaTaON_2$
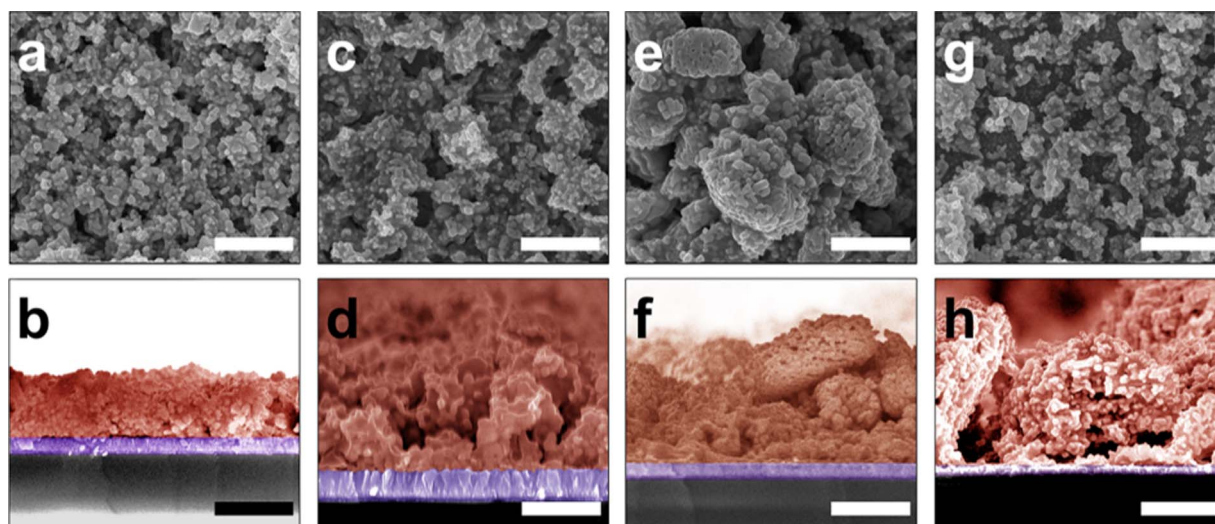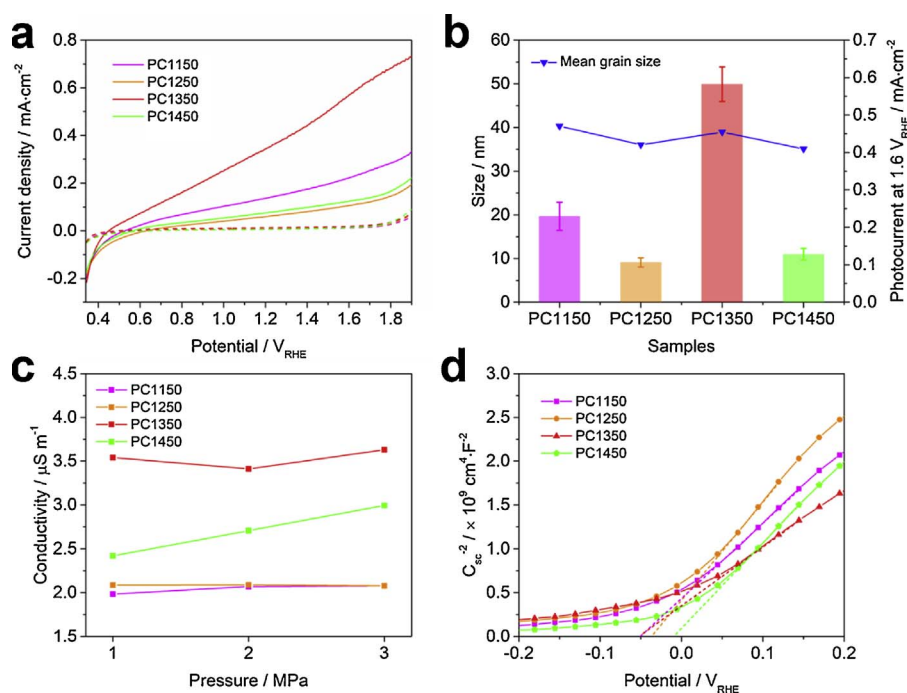


**Fig. 1.** SEM images of the particle-assembled photoanode films. The top row shows the surface of the photoanodes, while the bottom shows the corresponding cross sections. The scale bars are 2 μm. (a) and (b): PC1150; (c) and (d): PC1250; (e) and (f): PC1350; (g) and (h): PC1450.

**Fig. 2.** Photocurrent characteristics of LaTaON$_2$ photoanodes (a). The J-V measurements were carried out in 1 M NaOH electrolyte (pH = 13.6) under visible-light irradiation (a 500 W xenon lamp with a Hoya L-42 cut-off filter, $\lambda \geq 420$ nm). The scan rate was 30 mV/s. The dash lines show the dark-current of the corresponding LaTaON$_2$ photoanodes. Comparison of various samples and their corresponding photocurrents at 1.6 V$_{RHE}$ (b). The average (filled bars) photocurrents at 1.6 V$_{RHE}$ were extracted from the J-V measurements. The curve with blue inverted triangles stands for the mean grain sizes. Bulk electrical conductivity of LaTaON$_2$ powders under given pressures (c). Comparison of various LaTaON$_2$ samples with their corresponding flat band potentials and carrier densities (d). The Mott-Schottky tests were conducted in the dark with 1 M NaOH served as electrolyte. The frequencies were 1000 Hz, and the penetration amplitudes were 5 mV.
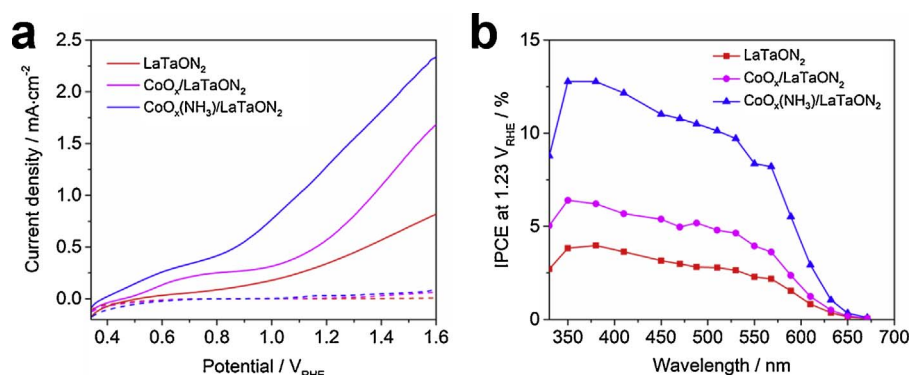
photoanodes.

To confirm the PEC performance of various photoanodes, Fig. S6 summarizes the corresponding photocurrents of 4 photoanodes at 1.6 V$_{RHE}$, with four each under the same testing conditions (more details can be found in Supporting Information). In addition, Na$_2$SO$_3$ was added to the electrolyte as a sacrificial agent [41]. A typical J-V plot is shown in Fig. S7a, with and without the sacrificial agent, under both back-side illumination (light/electrolyte/FTO/LaTaON$_2$) and front-side (light/electrolyte/LaTaON$_2$/FTO) illumination. Fig. S7b summarizes the photocurrents of all the photoanodes at 1.2 V$_{RHE}$. These experiments further support the fact that PC1350 possesses the best performance among these samples. In addition, the path for electron transport is still the limiting factor, as the photocurrent under back-side illumination is better than that under front-side illumination (as shown in Fig. S7b in Supporting Information). However, the photocurrent of the (oxy) nitride photoelectrodes without any surface modification usually decreases rapidly during operation. The case of the LaTaON$_2$ photoanodes is no exception (as shown in Fig. S16), and this deters the wide utilization of (oxy)nitride photoelectrodes. An attempt has been made to address this dilemma. CoO$_x$ was deposited on the photoanodes via photoelectrodeposition [46–50], and a post heat treatment under different atmospheres (air, N$_2$, and NH$_3$) was conducted [51].

Fig. 3a demonstrates the photocurrent of CoO$_x$-modified PC1350 photoanodes with and without post heat treatment under NH$_3$ in 1 M

NaOH under AM1.5G simulated sunlight. The catalyst layer deposited by photoelectrodeposition remarkably improves the photocurrent at high bias, from 0.8 mA cm$^{-2}$ to 1.6 mA cm$^{-2}$ at 1.6 V$_{RHE}$, while the onset potential is ca. 1.0 V$_{RHE}$. With another post heat treatment under NH$_3$, the corresponding photocurrent of the CoO$_x$-modified photoanode is further improved to 2.1 mA cm$^{-2}$ at 1.6 V$_{RHE}$, and the onset potential has a cathodic shift of 300 mV, from 1.0 to 0.7 V$_{RHE}$. However, under N$_2$ and air, these post heat treatments seem to be harmful to the CoO$_x$-modified photoanodes, as shown in Fig. S8a in Supporting Information. The post heat treatments under N$_2$ and air may create defects on the surface of the photoanodes, leading to impaired performance as shown in Fig. S8c. The curves in Fig. S8b show that the procedure is repeatable. The CoO$_x$ deposited on conductive substrates with and without the post heat treatment under different atmospheres possess similar oxygen evolution activity, as shown in Fig. S9 in Supporting Information.

The plot of the incident photon-to-current efficiency (IPCE) is shown in Fig. 3b. At 1.23 V$_{RHE}$, the bare LaTaON$_2$ photoanode shows an average of 3% incident photo-to-current conversion efficiency, which is increased to 6% for the CoO$_x$-modified anode without a post heat treatment. A further improvement to 12% has been achieved after the post heat treatment under NH$_3$. The integrated photocurrents were nearly the same with their corresponding value got under AM1.5 stimulated sunlight, suggesting the measured IPCE values are valid, as



**Fig. 3.** Photocurrent characteristics of different CoO$_x$-modified LaTaON$_2$ photoanodes (a) and comparison of IPCE for photoanodes with and without modification (b). In figure a, the J-V measurements were carried out in 1 M NaOH electrolyte (pH = 13.6) under AM 1.5 simulated sunlight (calibrated to 100 mW cm$^{-2}$, Oriel Sol3A Class AAA Solar Simulator). The dash lines show the dark-current of the corresponding LaTaON$_2$ photoanodes. In figure b, incident photon-to-current efficiency (IPCE) of CoO$_x$-modified LaTaON$_2$ photoanodes with and without post heat treatment under NH$_3$ compared with the bare photoanode at 1.23 V$_{RHE}$ in 1 M NaOH under back-side illumination.
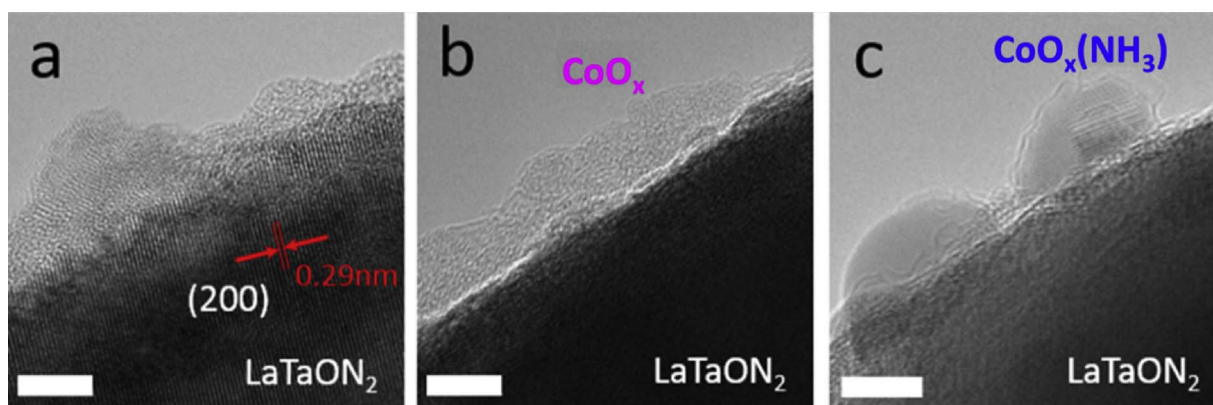
**Fig. 4.** HRTEM images of particles on the photoanodes. (a) A particle from an as-fabricated LaTaON$_2$ photoanode (PC1350). (b) A particle from CoO$_x$/LaTaON$_2$. (c) A particle from CoO$_x$(NH$_3$)/LaTaON$_2$. The spacing of 0.29 nm in Fig. 4a corresponding to the (2 0 0) plane of perovskite-type LaTaON$_2$. The scale bars are 5 nm.

shown in Fig. S10 in Supporting Information.

Because the CoO$_x$ with and without post heat treatments have similar oxygen evolution activity, the configuration and distribution of the oxygen evolution catalyst significantly influence the PEC performance of the photoanodes. Thus, SEM observation was conducted to the bare and CoO$_x$-modified LaTaON$_2$ photoanodes, both as deposited and with post heat treatment under NH$_3$. However, no obvious difference is seen. Only smooth surfaces with voids are observed, as shown in Fig. S11 in Supporting Information. In addition, similar Co mappings for these photoanodes are obtained, as shown in Fig. S12 in Supporting Information. This is mainly because the amount of oxygen evolution catalyst on them is at the detection limit (∼0.1%). But Co species do deposit on the photoanodes, confirmed by XPS, as shown in Fig. S13 in Supporting Information. With the help of the HRTEM images, the detail of the configuration and distribution of CoO$_x$ can be observed at the atomic scale.

As shown in Fig. 4a, the particle from the bare LaTaON$_2$ photoanode is covered with TiO$_x$, which is a mixture of amorphous and crystallized TiO$_x$, more details can be found in Fig. S14. The nanocrystalline TiO$_x$ particles are incorporated in the amorphous structure. No Co was detected from EDX (energy dispersive X-ray) detection mapping (not shown here). As for the CoO$_x$/LaTaON$_2$ photoanode, the Co species appears as a completely amorphous structure with a thickness of approximately 5 nm covering the particle (Fig. 4b). After a post heat treatment under NH$_3$, the amorphous CoO$_x$ layer recrystallized into nanospheres with a diameter of ca. 10 nm, as shown in Fig. 4c. Besides, the electrode with the CoO$_x$ nanospheres shows a higher carrier density than the amorphous electrode, as shown in Fig. S15b. However, in the case of CoO$_x$ as deposited, the onset potential has an anodic shift of 50 mV compared with the bare anode, from ca. 0.95 V$_{RHE}$ to 1.0 V$_{RHE}$, which may be due to inefficient hole separation at low bias. The recrystallized CoO$_x$ nanospheres accompanying with a greater part of the LaTaON$_2$ particle exposing to the electrolyte, which may facilitate the formation of Schottky nano-junctions [52,53], accelerated the hole separation at all bias values, thus the photocurrent is further increased with a 300 mV cathodic shift of the onset potential compared with the potential of the as-deposited CoO$_x$.

In the long-term test under simulated sunlight irradiation, the photocurrent of the bare PC1350 photoanode decays steeply to a negligible value in seconds with a large transient current, shown in Fig. S16. This steep decay is retarded after addition of the photoelectrodeposited CoO$_x$. After a post heat treatment under NH$_3$, a higher photocurrent is achieved accompanied by much better stability. The curves of current versus time at a given potential (1.23 V$_{RHE}$), represents the typical profile of (oxy)nitride photoanodes under operating conditions. The faradaic efficiencies for H$_2$ and O$_2$ evolution are 94% and 70%, respectively (as shown in Fig. S17 in Supporting Information). The reason for the relative lower faradaic efficiency for

O$_2$ evolution may be the amount of the evaluated O$_2$ that was dissolved in the electrolyte, which could not be detected by the micro GC, and the back reaction on the Pt foil. The slow kinetics of water oxidation could be responsible for this decay. Thus, a new kind of more efficient oxygen evolution catalyst should be introduced and a protective layer, such as amorphous TiO$_2$, should be deposited on these photoanodes. On the other hand, what has been happening to the (oxy)nitrides under operational conditions is still unknown. More details of the structure and interface should be investigated to determine the principal cause.

## 4. Conclusions

In conclusion, by synthesizing LaTaON$_2$ particles via flux-assisted ammonolysis of various precursors, the photoanodes of LaTaON$_2$ have achieved 0.8 mA cm$^{-2}$ at 1.6 V$_{RHE}$ in 1 M NaOH under AM1.5G simulated sunlight. The enhancement may be ascribed to increased bulk electrical conductivity and suppressed back reaction. CoO$_x$ is firstly deposited on the LaTaON$_2$ photoanode, and its photocurrent is enhanced dramatically after a heat treatment in NH$_3$, which results in the crystallized CoO$_x$ nanospheres on the LaTaON$_2$ particles. In addition, the configuration of dispersed crystallized CoO$_x$ nanospheres on particles promotes the forming of Schottky nano-junctions, which facilitate the charge separation compared with the amorphous CoO$_x$ layer. This study provides more details for the construction of highly efficient photoanodes that promote the utilization of (oxy)nitrides. Based on this study, an ideal configuration of the particle-assembled photoanode is proposed and shown in Fig. S18.

## Competing interests

The authors declare that they have no competing interests.

## Data and materials availability

All data needed to evaluate the conclusions in the paper are present in the paper and/or the Supplementary Materials. Additional data related to this paper may be requested from the authors.

## Appendix A. Supplementary data

Supplementary data associated with this article can be found, in the online version, at https://doi.org/10.1016/j.apcatb.2017.12.033.

## References

[1] A. Fujishima, K. Honda, Nature 238 (1972) 37–38.
[2] N.S. Lewis, D.G. Nocera, Proc. Natl. Acad. Sci. U. S. A. 103 (2006) 15729–15735.
[3] A.J. Nozik, Annu. Rev. Phys. Chem. 29 (1978) 189–222.
[4] O. Khaselev, J.A. Turner, Science 280 (1998) 425–427.
[5] M.G. Kibria, H.P.T. Nguyen, K. Cui, S. Zhao, D. Liu, H. Guo, M.L. Trudeau, S. Paradis, A.-R. Hakima, Z. Mi, ACS Nano 7 (2013) 7886–7893.
[6] M. Grätzel, Nature 414 (2001) 338–344.
[7] M.G. Walter, E.L. War-ren, J.R. McKone, S.W. Boettcher, Q. Mi, E.A. Santori, N.S. Lewis, Chem. Rev. 110 (2010) 6446–6473.
[8] Z. Li, W. Luo, M. Zhang, J. Feng, Z. Zou, Energy Environ. Sci. 6 (2013) 347–370.
[9] Z. Li, J. Feng, S. Yan, Z. Zou, Nano Today 10 (2015) 468–486.
[10] A. Kudo, Y. Miseki, Chem. Soc. Rev. 38 (2009) 253–278.
[11] J.Z. Zhang, MRS Bull. 36 (2011) 48–55.
[12] T. Bak, J. Nowotny, M. Rekas, C.C. Sorrell, Int. J. Hydrogen Energy 27 (2002) 991–1022.
[13] F.E. Osterloh, Chem. Mater. 20 (2008) 35–54.
[14] M.G. Kibria, Z. Mi, J. Mater. Chem. A 4 (2016) 2801–2820.
[15] B.D. Alexander, P.J. Kulesza, I. Rutkowska, R. Solarska, J. Augustynski, J. Mater. Chem. 18 (2008) 2298–2303.
[16] C. Santato, M. Ulmann, J. Augustynski, J. Phys. Chem. B 105 (2001) 936–940.
[17] J. Brillet, J.-H. Yum, M. Cornuz, T. Hisatomi, R. Solarska, J. Augustynski, M. Grätzel, K. Sivula, Nat. Photon. 6 (2012) 824–828.
[18] T. Zhang, Z. Zhu, H. Chen, Y. Bai, S. Xiao, X. Zheng, Q. Xue, S. Yang, Nanoscale 7 (2015) 2933–2940.
[19] K. Sayama, A. Nomura, Z. Zou, R. Abe, Y. Abe, H. Arakawa, Chem. Commun. 23 (2003) 2908–2909.
[20] F.F. Abdi, R. van de Krol, J. Phys. Chem. C 116 (2012) 9398–9404.
[21] W. Luo, Z. Yang, Z. Li, J. Zhang, J. Liu, Z. Zhao, Z. Wang, S. Yan, T. Yu, Z. Zou, Energy Environ. Sci. 4 (2011) 4046–4051.
[22] Y. Hu, Y. Su, H. Huang, Q. Qian, Z. Guan, J. Feng, Z. Li, Z. Zou, ChemCatChem 7 (2015) 2979–2985.
[23] I. Cesar, K. Sivula, A. Kay, R. Zboril, M. Grätzel, J. Phys. Chem. C 113 (2009) 772–782.
[24] S.D. Tilley, M. Cornuz, K. Sivula, M. Grätzel, Angew. Chem. Int. Ed. 122 (2010) 6549–6552.
[25] K. Sivula, F. Le Formal, M. Grätzel, ChemSusChem 4 (2011) 432–449.
[26] S.C. Warren, K. Voïtchovsky, H. Dotan, C.M. Leroy, M. Cornuz, F. Stellacci, C. Hébert, A. Rothschild, M. Grätzel, Nat. Mater. 12 (2013) 842–849.
[27] J.-W. Jang, C. Du, Y. Ye, Y. Lin, X. Yao, J. Thorne, E. Liu, G. McMahon, J. Zhu, A. Javey, J. Guo, D. Wang, Nat. Commun. 6 (2015) 7447.
[28] M. Zhang, W. Luo, Z. Li, T. Yu, Z. Zou, Appl. Phys. Lett. 97 (2010) 042105.
[29] D. Cao, W. Luo, J. Feng, X. Zhao, Z. Li, Z. Zou, Energy Environ. Sci. 7 (2014) 752–759.
[30] J. Feng, D. Cao, Z. Wang, W. Luo, J. Wang, Z. Li, Z. Zou, Chem. – Eur. J. 20 (2014) 16384–16390.
[31] C.M. Leroy, A.E. Maegli, K. Sivula, T. Hisatomi, N. Xanthopoulos, E.H. Otal, S. Yoon, A. Weidenkaff, R. Sanjines, M. Grätzel, Chem. Commun. 48 (2012) 820–822.
[32] K. Ueda, T. Minegishi, J. Clune, M. Nakabayashi, T. Hisatomi, H. Nishiyama, M. Katayama, N. Shibata, J. Kubota, T. Yamada, K. Domen, J. Am. Chem. Soc. 137 (2015) 2227–2230.
[33] L. Zhang, Y. Song, J. Feng, T. Fang, Y. Zhong, Z. Li, Z. Zou, Int. J. Hydrogen Energy 39 (2014) 7697–7704.
[34] P. Sarkar, P.S. Nicholson, J. Am. Ceram. Soc. 79 (1996) 1987–2002.
[35] O.O. Van der Biest, L.J. Vandeperre, Annu. Rev. Mater. Sci. 29 (1999) 327–352.
[36] N.-Y. Park, Y.-I. Kim, J. Mater. Sci. 47 (2012) 5333–5340.
[37] Y.-I. Kim, Doctoral Thesis, The Ohio State University, 2005.
[38] Y.-I. Kim, Ceram. Int. 40 (2014) 5275–5281.
[39] M. Jansen, H.P. Letschert, Nature 404 (2000) 980–982.
[40] M. Liu, W. You, Z. Lei, T. Takata, K. Domen, C. Li, Chin. J. Catal. 27 (2006) 556–558.
[41] J. Feng, W. Luo, T. Fang, H. Lv, Z. Wang, J. Gao, W. Liu, T. Yu, Z. Li, Z. Zou, Adv. Funct. Mater. 24 (2014) 3535–3542.
[42] Z. Lyu, D. Xu, L. Yang, R. Che, R. Feng, J. Zhao, Y. Li, Q. Wu, X. Wang, Z. Hu, Nano Energy 12 (2015) 657–665.
[43] D. Eisenberg, H.S. Ahn, A.J. Bard, J. Am. Chem. Soc. 136 (2014) 14011–14014.
[44] Z. Chen, T.F. Jaramillo, T.G. Deutsch, A. Kleiman-Shwarsctein, A.J. Forman, N. Gaillard, R. Garland, K. Takanabe, C. Hesk, M. Sunkara, E.W. McFarlan, K. Domen, E.L. Miller, J.A. Turner, H.N. Dinh, J. Mater. Res. 25 (2010) 3–16.
[45] W. Luo, Z. Li, T. Yu, Z. Zou, J. Phys. Chem. C 116 (2012) 5076–5081.
[46] D.K. Zhong, M. Cornuz, K. Sivula, M. Grätzel, D.R. Gamelin, Energy Environ. Sci. 4 (2011) 1759–1764.
[47] T.W. Kim, K.-S. Choi, Science 343 (2014) 990–994.
[48] R.N. Dominey, N.S. Lewis, J.A. Bruce, D.C. Bookbinder, M.S. Wrighton, J. Am. Chem. Soc. 104 (1982) 467–482.
[49] L. Martinez, D. Leinen, F. Martín, M. Gabas, J.R. Ramos-Barrado, E. Quagliata, E.A. Dalchiele, J. Electrochem. Soc. 154 (2007) D126–D133.
[50] G.K. Schweitzer, L.L. Pesterfield, The Aqueous Chemistry of the Elements, Oxford University Press, 2010.
[51] A.E. Maegli, S. Pokrant, T. Hisatomi, M. Trottmann, K. Domen, A. Weidenkaff, J. Phys. Chem. C 118 (2014) 16344–16351.
[52] Y. Ping, W.A. Goddard III, G.A. Galli, J. Am. Chem. Soc. 137 (2015) 5264–5267.
[53] D. Ding, K. Liu, S. He, C. Gao, Y. Yin, Nano Lett. 14 (2014) 6731–6736.